ChemPubSoc Europe

DOI: 10.1002/cmdc.201700718

CHEMMEDCHEM Full Papers

Discovery of Rogaratinib (BAY 1163877): a pan-FGFR Inhibitor

Marie-Pierre Collin,*[a] Mario Lobell,[a] Walter Hübsch,[a] Dirk Brohm,[a] Hartmut Schirok,[a] Rolf Jautelat,[a] Klemens Lustig,[c] Ulf Bömer,[d] Verena Vöhringer,[b] Mélanie Héroult,[b] Sylvia Grünewald,[b] and Holger Hess-Stumpp[b]

Rogaratinib (BAY 1163877) is a highly potent and selective small-molecule pan-fibroblast growth factor receptor (FGFR) inhibitor (FGFR1–4) for oral application currently being investigated in phase 1 clinical trials for the treatment of cancer. In this publication, we report its discovery by de novo structure-based design and medicinal chemistry optimization together with its pharmacokinetic profile.

Introduction

Fibroblast growth factors (FGFs) and their transmembrane tyrosine kinase receptors play an important role in tissue homeostasis during embryonic development and adulthood.[1] It has been found that FGF signaling is affected by multiple mechanisms: gene amplifications, activating mutations, chromosomal translocations, single nucleotide polymorphisms and aberrant splicing at the post-transcriptional level.[2] Because of the strong link between aberrant FGFR signaling and carcinogenesis, FGFR inhibition appears to be an innovative approach for new cancer therapies.

Several specific orally bioavailable small-molecule inhibitors of FGFR are currently in clinical development (Figure 1).[3] The acylaminopyrazole AZD4547 is a pan-FGFR inhibitor (in vitro IC_{50} values of 0.2, 2.5, and 1.8 nM against FGFR-1, FGFR-2, and FGFR-3, respectively) exhibiting selectivity against VEGFR-2 (also known as KDR, IC_{50} = 24 nM). It is under investigation in phase II/III clinical trials for the treatment of squamous cell lung cancer.[4]

JNJ-42756493 is a quinoxaline pan-FGFR inhibitor (FGFR1–4 $IC_{50} \approx 1$ nM; VEGFR kinase selectivity ~20-fold) with ongoing development in a phase I/II clinical study for the treatment of urothelial cancer.[5]

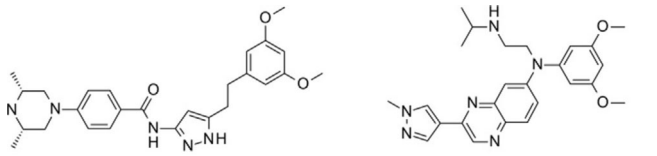

Figure 1. Selected pan-FGFR inhibitors under investigation in clinical trials.

We set out to identify a novel chemotype for selective inhibition of the FGFR kinases with a favorable drug metabolism and pharmacokinetic (DMPK) profile for oral application. The selectivity versus VEGFR-2 was an important optimization parameter in order to improve the tolerability related to VEGFR-2-mediated side effects. The FGFR inhibitor project started with a de novo structure-based design approach.

In 2015 Hillisch et al. described how computational chemistry has significantly and positively impacted the clinical development pipeline of the pharmaceutical industry in general, and Bayer in particular.[6] In that report, we referred to successful examples of de novo structure-based design leading to clinical candidates. Herein we report one of such yet unpublished examples, namely the lead discovery and optimization program leading to rogaratinib, a potent and selective FGFR1–4 inhibitor.

Results and Discussion

Design of 5-benzothiophene-pyrrolotriazine

At the time this work was performed X-ray crystal structures of the FGFR kinase domain had only been published for isoform 1 and not for isoforms 2, 3, or 4. Between the four isoforms there are no mutations within 5 Å of the ATP binding site except for the Y566C mutation in FGFR4. For this reason it was seen as acceptable to do all modeling with one of the published FGFR1 X-ray crystal structures. The starting point of the structure-based design approach was a WaterMap analysis of the FGFR-1 ATP binding site (PDB ID: 2FGI, active DFG-in

[a] Dr. M.-P. Collin, Dr. M. Lobell, Dr. W. Hübsch, Dr. D. Brohm, Dr. H. Schirok, Dr. R. Jautelat
Department of Medicinal Chemistry, Drug Discovery, Bayer AG, Postfach 101709, 42096 Wuppertal (Germany)
E-mail: marie-pierre.collin@bayer.com

[b] Dr. V. Vöhringer, Dr. M. Héroult, Dr. S. Grünewald, Dr. H. Hess-Stumpp
Therapeutic Research Group, Oncology, Drug Discovery, Bayer AG (Germany)

[c] Dr. K. Lustig
Research Pharmacokinetics Group, Drug Discovery, Bayer AG (Germany)

[d] Dr. U. Bömer
Lead Discovery, Drug Discovery, Bayer AG (Germany)

Supporting information and the ORCID identification number(s) for the author(s) of this article can be found under: https://doi.org/10.1002/cmdc.201700718.

kinase form).[7] WaterMap is a software tool from Schrödinger, which performs mapping of the locations and thermodynamic properties of water molecules that solvate a protein binding site.[8,9] Displacement of high-energy water molecules by a ligand should contribute to its binding affinity. One can therefore use the locations of high-energy water molecules in a calculated water map to guide de novo ligand design as illustrated in Figure 2. ATP-competitive kinase inhibitors usually form

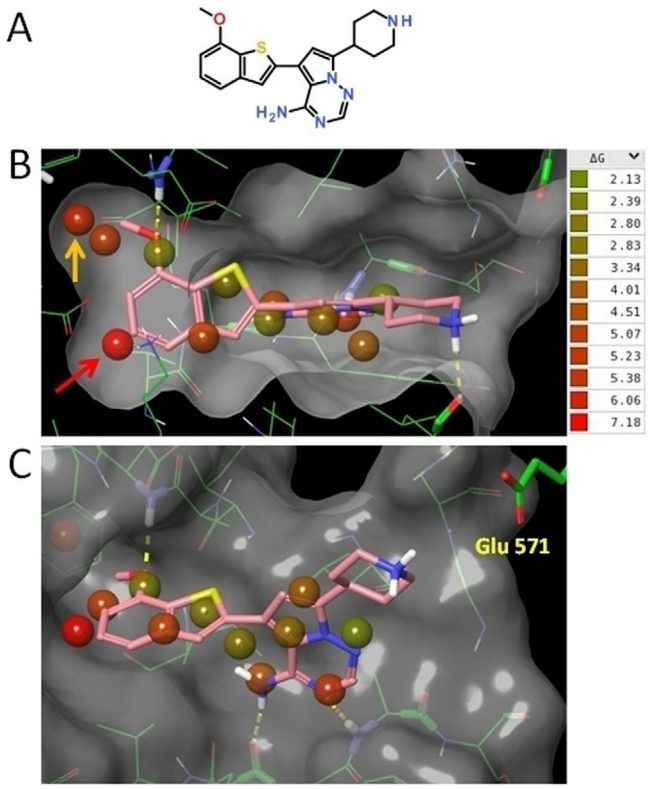

Figure 2. A) Chemical structure of compound **1**. B) Top view of ATP binding site in FGFR-1 (green C atoms, semitransparent grey surface) with docked compound **1** (pink C atoms) and overlayed hydration sites calculated by WaterMap. Only the energetically most unfavorable hydration sites with the highest calculated free energy ($\Delta G > 2$ kcal mol^{-1}) are shown as spheres colored from green (near 2 kcal mol^{-1}) to red (near 7 kcal mol^{-1}), the two highest-energy hydration sites are indicated by a red (7.2 kcal mol^{-1}) and orange (6.1 kcal mol^{-1}) arrow. Predicted hydrogen bonds between the inhibitor and the protein are shown as yellow broken lines. C) Same as panel B, but side view with front parts of the protein removed for clarity. The side chain of Glu571 is shown without a semitransparent grey surface in the upper right-hand corner.

one to three hydrogen bonds to the so-called kinase hinge region, which offers a triad of potential hydrogen bonding partners via backbone carbonyl acceptor, NH donor, and carbonyl acceptor. In a first design step, a virtual in-house collection of various heterocyclic scaffolds were docked for evaluation as potential hinge binders. Among several possible heterocyclic core structures, the aminopyrrolotriazine core was selected as the most promising scaffold. It provided hinge binding with two hydrogen bonds and suitable attachment vectors to place a head group into the hydrophobic back pocket of FGFR-1 and a solubilizing tail group directed toward a solvent region. In an effort to displace many of the unfavorable high-energy water molecules calculated by WaterMap, a 7-alkoxybenzothiophene head group in the 5-position of the pyrrolotriazine was proposed. The five-membered thiophene ring provides exactly the desired vectors needed to position the phenyl ring of the benzothiophene in a central position in the back pocket and enables the alkoxy substituent to enter a deep subpocket, forming a hydrogen bond to the backbone NH of Asp641. An additional piperidinyl group was attached to enhance water solubility, leading to compound **1** (Figure 2).

Compound **1** was synthesized and tested in the biochemical FGFR-1 assay with low ATP (10 μM) and high ATP (2 mM) concentrations, yielding IC_{50} values of 48 nM (low ATP) and 115 nM (high ATP). Some selectivity was observed versus VEGFR-2 with an IC_{50} value of 823 nM at low ATP concentration (Table 1). In our cellular FGFb-stimulated HUVEC proliferation assay, compound **1** showed an IC_{50} value of 1.1 μM. The already appealing biochemical and cellular FGFR inhibitory potency of our first compound combined with some selectivity toward VEGFR-2 encouraged us to further optimize this lead structure.

Medicinal chemistry optimization

Starting with the optimization of the head group, analysis of the FGFR-1 crystal structure indicated two areas for potential improvement. Introducing a lipophilic substituent at C5 of the benzothiophene group should fill a hydrophobic back pocket, fully displacing the highest-energy hydration site, indicated by a red arrow in Figure 2. Based on the above-mentioned hypothesis, the 5-methylbenzothiophene **2** was synthesized (Table 1). In vitro testing showed that despite the absence of the C7 methoxy group, introduction of a methyl group at position C5 of the benzothiophene maintained FGFR-1 potency (compound **2**, $IC_{50} = 86$ nM). 5-Fluoro (**3**), 5-trifluoromethyl (**4**), and 5-trifluoromethoxy (**5**) analogues were significantly weaker. Elongation of the methoxy group promised to replace an additional high-energy hydration site indicated by the orange arrow in Figure 2B. However, replacement of the methoxy group by a trifluoroethoxy substituent (**6**) resulted in decreased rather than the anticipated increased activity (Table 1).

Later attempts with an ethoxy or fluoroethoxy group in combination with a different tail group also led to derivatives with decreased activity (discussed below in greater detail). Further variation around the benzothiophene moiety demonstrated that benzothiophene was the most favorable substituent. Indeed, its replacement by a naphthyl (**8**) or benzofuran (**9**) group led to lower FGFR-1 activity. Finally, combination of the 5-methyl and 7-methoxy substituents resulted in a favorable additive effect on FGFR activity (compound **10**: $IC_{50} = 4$ nM) and represented a major breakthrough in the lead optimization.

To optimize the tail group, we tried to exploit a structural difference in the ATP binding site. Glutamic acid 571 (Glu571) of the FGFR-1 ATP binding site is exchanged for a threonine in the corresponding position in VEGFR-2. We hoped to create a beneficial ligand interaction with Glu571 to enhance FGFR-1 potency and VEGFR-2 selectivity. The insertion of a methylene

Table 1. Selected R^A substituents and their effect on potency toward FGFR-1 and VEGFR-2.

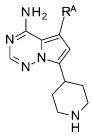

Compd	R^A	FGFR-1 IC_{50} [nM][a]*	VEGFR-2 IC_{50} [nM][b]#	Compd	R^A	FGFR-1 IC_{50} [nM][a]*	VEGFR-2 IC_{50} [nM][b]#
1		115	823	**6**	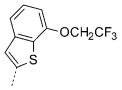	838#	n.d.
2	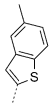	86	116	**7**		319	152
3	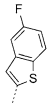	567	n.d.	**8**		526	273
4	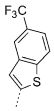	940	n.d.	**9**		3740	> 20000
5	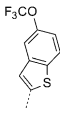	3770#	n.d.	**10**	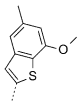	4	62

[a] Determined by biochemical FGFR-1 activity inhibition assay. [b] Determined by biochemical VEGFR-2 activity inhibition assay. See Supporting Information for further details. *High ATP = 2 mM, #Low ATP = 10 μM; n.d. = not determined.

group between the pyrrolotriazine core and a piperazine tail group was predicted to allow the desired hydrogen bond interaction with the side chain of Glu571 (Figure 3).

In fact, compound **11**, with a 7-piperazinylmethyl substituent retained FGFR potency and diminished VEGFR-2 activity relative to its piperidine counterpart **1** (Table 2). Broad derivatization of the tail group (Table 2) furnished further interesting compounds with a 3-pyrrolidine (**12**) or a morpholinomethyl moiety (**13**). Compound **15**, a more flexible open-chain analogue of piperazine **11** had weaker FGFR-1 activity. A straightforward combination of the most promising head and tail groups afforded our lead candidate compound **18** (Table 3). Potency, selectivity, and key pharmacokinetic properties of compound **18** are listed in Tables 3 and 4. The pyrrolotriazine **18** is a potent FGFR-1 and FGFR-3 inhibitor with good cellular potency. The VEGFR-2 selectivity of this compound was also improved. Docking of compound **18** in FGFR-1 is illustrated in Figure 3. In vivo pharmacokinetic investigations of pyrrolotriazine **18** in rat showed low clearance, but only low to moderate bioavailability (Table 4).

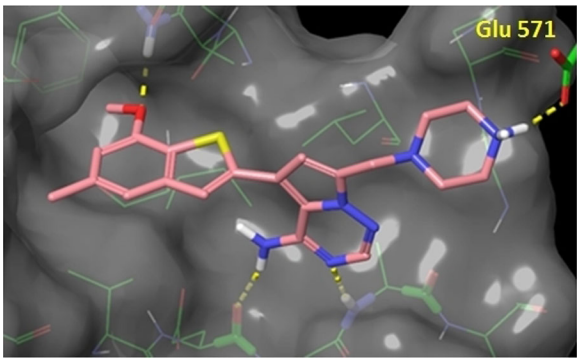

Figure 3. Side view of ATP binding site in FGFR-1 (green C atoms, semitransparent grey surface) with docked compound **18** (pink C atoms). Predicted hydrogen bonds between the inhibitor and the protein are shown as yellow broken lines. The carboxylate moiety of Glu571 is shown without a semitransparent grey surface in the upper right-hand corner. Front parts of the protein have been removed for clarity.

During the lead optimization phase, the head group was further investigated. Replacing the benzothiophene group by a thiophene carboxylic acid or its corresponding ethyl ester (Table 5, compounds **23** and **24**) resulted in a significant loss of potency.

Compound **20** showed good FGFR potency paired with high VEGFR-2 selectivity; however, in vitro hepatocyte clearance was very high (3.4 $L\,h^{-1}\,kg^{-1}$), probably due to conjugative phase II metabolism involving the hydroxy group. To address the lipophilic back pocket, the 5-chlorobenzothiophene analogue **25** was synthesized and surprisingly did not quite achieve the activity level of our lead compound **18** (compound **25** IC_{50} = 35 nM). Elongation of the C7 substituents did not improve the FGFR potency (compounds **26**, **27**, and **28**) in contradiction with modeling predictions based on the WaterMap analysis.

We hypothesized that the basic secondary amine moiety of compound **18** (exp. $pK_a = 9.1$) was responsible for the active

Table 2. Selected R^B substituents and their effect on FGFR-1 and VEGFR-2 potency.

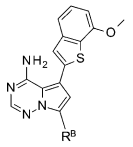

Compd	R^B	FGFR-1 IC_{50} [nM][a]*	VEGFR-2 IC_{50} [nM][b]#	Compd	R^B	FGFR-1 IC_{50} [nM][a]*	VEGFR-2 IC_{50} [nM][b]#
1		115	823	**14**		214	109
11		93	3030	**15**		376	1100
12		88	215	**16**	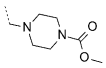	588	n.d.
13		124#	1300	**17**		629	n.d.

[a] Determined by biochemical FGFR-1 activity inhibition assay. [b] Determined by biochemical VEGFR-2 activity inhibition assay. See Supporting Information for further details. *High ATP = 2 mM, #Low ATP = 10 μM; n.d. = not determined.

Table 3. FGFR and VEGFR-2 potency of the lead candidate **18**.

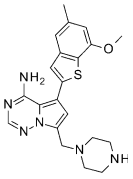

Biochemical assay IC_{50}	FGFR-1 (high ATP*)[a]	10 nM
	FGFR-3 (low ATP#)[b]	25 nM
	VEGFR-2 (low ATP#)[c]	846 nM
Proliferation assay IC_{50}	FGFb-stimulated HUVEC proliferation[d]	36 nM
	VEGF-stimulated HUVEC proliferation[e]	2.0 μM
	Selectivity ratio: VEGF/FGFb	56

[a] Determined by biochemical FGFR-1 activity inhibition assay. [b] Determined by biochemical FGFR-3 activity inhibition assay. [c] Determined by biochemical VEGFR-2 activity inhibition assay. [d] Inhibitory potency of endothelial cell growth stimulated by FGFb. [e] Inhibitory potency of endothelial cell growth stimulated by VEGF. See Supporting Information for further details. *High ATP = 2 mM, #Low ATP = 10 μM.

Table 4. Rat in vivo pharmacokinetic parameters after intravenous (i.v.) and oral (p.o.) application of lead candidate **18**.[a]

i.v. [1 mg kg^{-1}]		p.o. [3 mg kg^{-1}]	
CL_{bl}	0.45 L h^{-1} kg^{-1}	AUC_{norm}	0.78 kg h^{-1} L^{-1}
$V_{ss,pl}$	5.5 L kg^{-1}	$t_{1/2}$	12 h
$t_{1/2}$	12 h	F	22%

[a] 5 mL kg^{-1}; vehicle: plasma/DMSO = 99:1 (i.v.: 15 min infusion) or Solutol®/ethanol/water = 40:10:50 (p.o.); CL_{bl} = clearance blood, $V_{ss,pl}$ = volume of distribution at steady state in plasma, $t_{1/2}$ = half-life, AUC_{norm} = dose-normalized (1 mg kg^{-1}) area under the curve, F = absolute oral bioavailability. See Supporting Information for further details.

transporter efflux in the Caco-2 assay ($P_{app(A\rightarrow B)} = 38$ nm s^{-1}, efflux ratio (ER) = 4) explaining the low oral bioavailability. This hypothesis was supported by the high ERs of compounds **30** and **31** (Table 6, ERs of > 28 and 13, respectively). As a consequence, tail groups with decreased basicity were conceived. Introduction of a carbonyl group in the piperazine ring or replacement of the piperazine moiety by an aminopyrrolidinone group would fulfill this criterion and was in agreement with modeling considerations (Figure 4). Surprisingly, N-acetylation of the piperazine ring also led to a quite active and more permeable compound (**37**: Caco-2 $P_{app(A\rightarrow B)} = 241$ nm s^{-1}; ER = 1). The rather small loss of activity of the *N*-acetyl analogue **37** relative to piperazine **18** or piperazinone **38** indicates that the hypothesized hydrogen bond interaction with the side chain of Glu571 is not essential to achieve good potency. These structural alterations improved the permeation profile (decrease in ER; **38**: Caco-2 $P_{app(A\rightarrow B)} = 314$ nm s^{-1}; ER = 2) but also slightly

Table 5. Selected R^A substituents and their effect on FGFR-1 and VEGFR-2 potency.

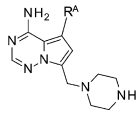

Compd	R^A	FGFR-1 IC_{50} [nM][a]*	VEGFR-2 IC_{50} [nM][b]#	Compd	R^A	FGFR-1 IC_{50} [nM][a]*	VEGFR-2 IC_{50} [nM][b]#	Compd	R^A	FGFR-1 IC_{50} [nM][a]*	VEGFR-2 IC_{50} [nM][b]#
18	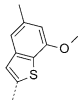	10	846	**22**	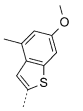	962	n.d.	**26**	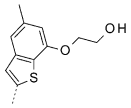	203	n.d.
19		227	>20000	**23**		8190	n.d.	**27**	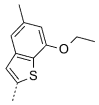	241	n.d.
20	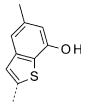	12	>20000	**24**		>20000	n.d.	**28**	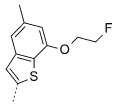	144	n.d.
21		165	n.d.	**25**	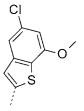	35	2540	**29**	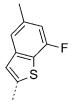	447	n.d.

[a] Determined by biochemical FGFR-1 activity inhibition assay. [b] Determined by biochemical VEGFR-2 activity inhibition assay. See Supporting Information for further details. *High ATP = 2 mM, #Low ATP = 10 μM; n.d. = not determined.

Table 6. Selected R^B substituents and their effect on FGFR-1 and VEGFR-2 potency as well as cellular activity, representative examples out of 368 analogues in total.

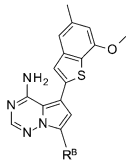

Compd	R^B	FGFR-1 IC_{50} [nM][a]*	FGFR Prolif. IC_{50} [nM][b]	VEGFR-2 IC_{50} [nM][c]#	Compd	R^B	FGFR-1 IC_{50} [nM][a]*	FGFR Prolif. IC_{50} [nM][b]	VEGFR-2 IC_{50} [nM][c]#
18		10	36	846	**35**		95	21	221
30	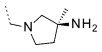	1.1	48	388	**36**		20	127	795
31	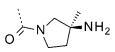	2.2	66	5930	**37**	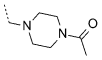	40	74	114
32		221	n.d.	n.d.	**38**		29	370	231
33		20	22	197	**39**		287	n.d.	n.d.
34		18	217	1100	**40**		37	166	527

[a] Determined by biochemical FGFR-1 activity inhibition assay. [b] Inhibitory potency of endothelial cell growth stimulated by FGFb. [c] Determined by biochemical VEGFR-2 activity inhibition assay. See Supporting Information for further details. *High ATP = 2 mM, #Low ATP = 10 μM; n.d. = not determined.

decreased the FGFR potency (Table 6). The most promising substituents were the aminopyrrolidinone **33** and the piperazinone **38** (Figure 4).

In parallel, examination of the crystal structure with docked compound **18** revealed that the cavity around C6 of the pyrrolotriazine core structure could tolerate an additional substituent with polar or lipophilic properties. C6-substituted analogues have their FGFR-1 activity significantly increased both in the biochemical and cellular assays (Table 7). Lipophilic substituents can improve potency via hydrophobic interactions

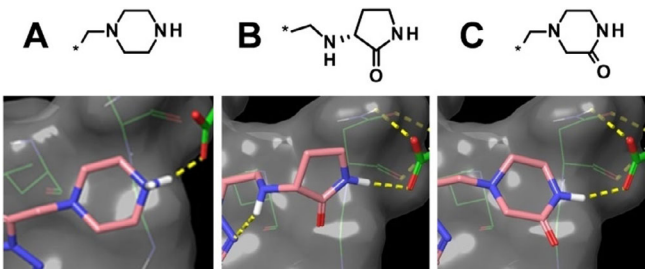

Figure 4. Docking images of the tail groups of compound **18** (A) and two non-basic cyclic amide moieties (B and C) capable of maintaining the hydrogen bonding donor interaction to Glu571 as proposed by modeling. Predicted hydrogen bonds are shown as yellow broken lines. The carboxylate moiety of Glu571 is shown without a semitransparent grey surface in the upper right-hand corner.

with the protein (Figure 5, supported, for example, by compounds **42**–**49** in Table 7). On the other hand, compounds with polar substituents (e.g., **41**, **50**, **51**, **54**, **55**, **60**–**62**, **74**) also demonstrated high FGFR potency, thus corroborating the previous modeling hypothesis (Figure 6). Unfortunately, combining the side chains at C6 with the piperazine tail group led to a decrease in permeability and an increase in efflux (e.g., **41**–**43**, **49**–**52**, **68**; Table 7) relative to the lead structure **18**.

As next step, the non-basic groups at C7 were combined with a variety of C6 substituents, hoping to overcome the permeation/efflux issue, in line with our hypothesis that basic amine moieties should be avoided. The combination of small ether side chains at the 6-position with the 7-piperazinonylmethyl residue afforded the most promising compounds. Among these derivatives, rogaratinib (**75**; Table 8) was chosen as the clinical candidate. Rogaratinib showed improved FGFR potency both in the biochemical and cellular proliferation assay, as well as a significantly enhanced permeation profile over the lead candidate **18**. Rogaratinib inhibits FGFR1–4 kinase activity in the nanomolar range. In HUVEC proliferation

Table 7. Representative selection of derivatives bearing side chains at C6 of the pyrrolotriazine and effect on FGFR potency and permeation (Caco-2).

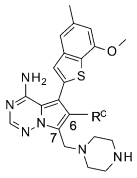

Compd	R^C	FGFR-1 IC_{50} [nM][a]	FGFR Prolif. IC_{50} [nM][b]	Caco-2 $P_{app(A\rightarrow B)}$ [$nm\,s^{-1}$]/ER[c]	Compd	R^C	FGFR-1 IC_{50} [nM][a]	FGFR Prolif. IC_{50} [nM][b]	Caco-2 $P_{app(A\rightarrow B)}$ [$nm\,s^{-1}$]/ER[c]
41	$-CH_2OH$	3.3	37	9/35	**60**	$-CH_2NH_2$	3.1	255	n.d.
42	$-CH_2OMe$	0.9	27	8/33	**61**	$-CH_2NHMe$	3.0	255	n.d.
43	$-CH_2OEt$	0.7	10	12/27	**62**	$-CH_2NHEt$	6.9	213	n.d.
44	$-CH_2OPr$	1.3	32	n.d.	**63**	$-CH_2NMe_2$	22	n.d.	n.d.
45	$-CH_2OBu$	18	n.d.	n.d.	**64**		3.2	85	n.d.
46	$-CH_2OiPr$	1.3	121	n.d.	**65**		1.7	107	n.d.
47		0.9	57	n.d.	**66**		2.1	157	n.d.
48		0.7	110	n.d.	**67**	$-CH_2NEt_2$	8.6	307	n.d.
49	$-CH_2OCH_2CF_3$	1.6	55	8/9	**68**	$-CH_2NHCH_2CH_2OH$	1.1	365	$<2/>23$
50	$-CH_2OCH_2CH_2NH_2$	2.8	375	$<5/>9$	**69**		3.4	171	n.d.
51	$-CH_2OCH_2CH_2OH$	0.9	78	$<1/>168$	**70**		5.1	305	n.d.
52	$-CH_2OCH_2CH_2OMe$	2.1	140	4/61	**71**		2.8	96	n.d.
53		0.5	865	n.d.	**72**		2.1	83	n.d.
54	$-CH_2OCH_2CO_2H$	5.2	2740	n.d.	**73**	$-CH_2NHCH_2CO_2H$	13	360	n.d.
55	$-CH_2OCH_2CONH_2$	1.0	n.d.	n.d.	**74**	$-CH_2NHAc$	1.0	n.d.	n.d.
56	$-CH_2OPh$	61	n.d.	n.d.					
57	$-Me$	3.7	47	n.d.					
58	$-Et$	2.2	25	n.d.					
59	$-Cl$	26	126	n.d.					

[a] Determined by biochemical FGFR-1 activity inhibition assay, ATP = 2 mM. [b] Inhibitory potency of endothelial cell growth stimulated by FGFb. [c] Transport rate of compound across Caco-2 cell monolayer; $P_{app(A\rightarrow B)}$ = transport in apical to basolateral direction; ER = efflux ratio (A→B/B→A). See Supporting Information for further details; n.d. = not determined.

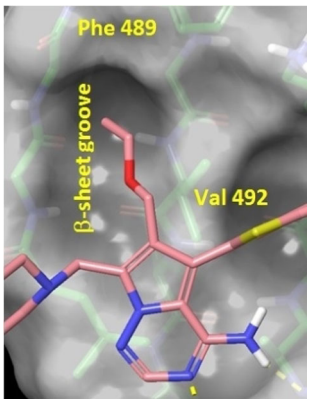

Figure 5. Side view of ATP binding site in FGFR-1 (green C atoms, semitransparent grey surface) with docked compound **43** (pink C atoms). Predicted hydrogen bonds are shown as yellow broken lines. Front parts of the protein have been removed for clarity. The ethoxy group is predicted to make beneficial interactions with a hydrophobic patch, which is formed by the β-sheet groove of the P-loop (also called glycine-rich loop) and the side chains of Phe489 and Val492.

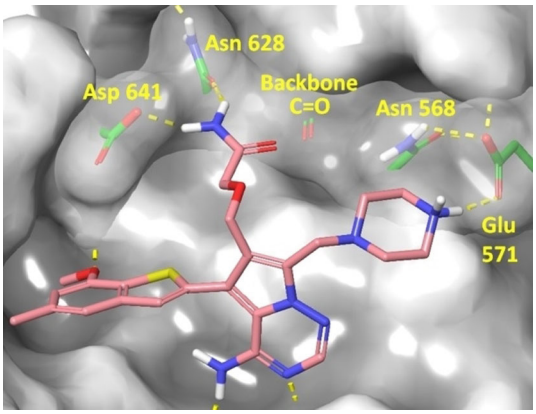

Figure 6. Side view of ATP binding site in FGFR-1 (some selected parts of the protein are shown as a stick model with green C atoms and a semitransparent grey surface including yellow labels, the rest as a solid grey surface) with docked compound **55** (stick model with pink C atoms). Predicted hydrogen bonds are shown as yellow broken lines. Front parts of the protein have been removed for clarity. The primary amide is predicted to make hydrogen bonds to the side chains of Asn628 and Asp641. These two side chains and the backbone carbonyl group of Arg627 form a triad of potential hydrogen bond acceptors available for interaction with suitably placed hydrogen bond donors of inhibitors.

assays, rogaratinib potently inhibits FGFb-stimulated HUVEC proliferation and demonstrates selectivity against VEGF-stimulated growth (VEGF/FGFb selectivity ratio = 28). Rogaratinib has a good pharmacokinetic profile after intravenous and oral application. The A→B permeation is 130 nm s^{-1} with a low efflux ratio (ER = 4). In vivo, rogaratinib showed low clearance and a moderate bioavailability in both rat and dog (Table 9).

Synthesis of rogaratinib (BAY 1163877)

Rogaratinib was prepared from the corresponding 6-methoxymethylpyrrolotriazine **83** (Scheme 1). It was planned to introduce the oxo-piperazine group by reductive amination and the

Table 8. FGFR potency, VEGFR-2 selectivity, and DMPK parameters of rogaratinib (**75**).

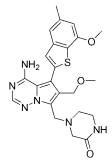

Biochemical assay IC_{50} [nM]	FGFR-1 (high ATP*)[a]		12
	FGFR-1 (low ATP#)[a]		15
	FGFR-2 (low ATP#)[b]		< 1
	FGFR-3 (low ATP#)[c]		19
	FGFR-4 (low ATP#)[d]		33
	VEGFR-2 (low ATP#)[e]		120
		Inhib. [%] @100 nM **75**	K_d [nM]
Competition binding assay[f]	FGFR-1	97	1.6
	FGFR-2	97	5.0
	FGFR-3	96	7.8
	FGFR-4	99	7.6
	VEGFR-2	19	–
Proliferation assay IC_{50}	FGFb-stimulated HUVEC proliferation[g]		16 nM
	VEGF-stimulated HUVEC proliferation[h]		453 nM
	Selectivity ratio: VEGF/FGFb		28

[a] Determined by biochemical FGFR-1 activity inhibition assay. [b] Determined by biochemical FGFR-2 activity inhibition assay at MerckMillipore (see Supporting Information for further details). [c] Determined by biochemical FGFR-3 activity inhibition assay. [d] Determined by biochemical FGFR-4 activity inhibition assay. [e] Determined by biochemical VEGFR-2 activity inhibition assay. [f] Active site-directed competition binding assay at DiscoverX.[10] [g] Inhibitory potency of endothelial cell growth stimulated by FGFb. [h] Inhibitory potency of endothelial cell growth stimulated by VEGF. See Supporting Information for further details. *High ATP = 2 mM, #Low ATP = 10 μM.

Table 9. DMPK parameters of rogaratinib (**75**).

		i.v.[a]		p.o.[a]
		0.5 mg kg^{-1}		5 mg kg^{-1}
rat	CL_{bl}	0.78 L h^{-1} kg^{-1}	AUC_{norm}	0.96 kg h^{-1} L^{-1}
	$V_{ss,pl}$	0.54 L kg^{-1}	$t_{1/2}$	4.5 h
	$t_{1/2}$	0.9 h	F	46%
		0.5 mg kg^{-1}		1 mg kg^{-1}
dog	CL_{bl}	0.36 L h^{-1} kg^{-1}	AUC_{norm}	1.2 kg h^{-1} L^{-1}
	$V_{ss,pl}$	1.2 L kg^{-1}	$t_{1/2}$	3.8 h
	$t_{1/2}$	3.1 h	F	35%

[a] 5 mL kg^{-1}; vehicle: plasma/DMSO = 99:1 (rat i.v.: 15 min infusion); PEG400/ethanol/water/HCl (1 M) = 20:5:74.5:0.5 (dog i.v.: 15 min infusion); PEG400/ethanol/water = 40:10:50 (rat p.o.: gavage); PEG400/ethanol/water = 20:5:75 (dog p.o.: gavage); CL_{bl} = clearance blood, $V_{ss,pl}$ = volume of distribution at steady state in plasma, $t_{1/2}$ = half-life, AUC_{norm} = dose-normalized (1 mg kg^{-1}) area under the curve, F = absolute oral bioavailability.

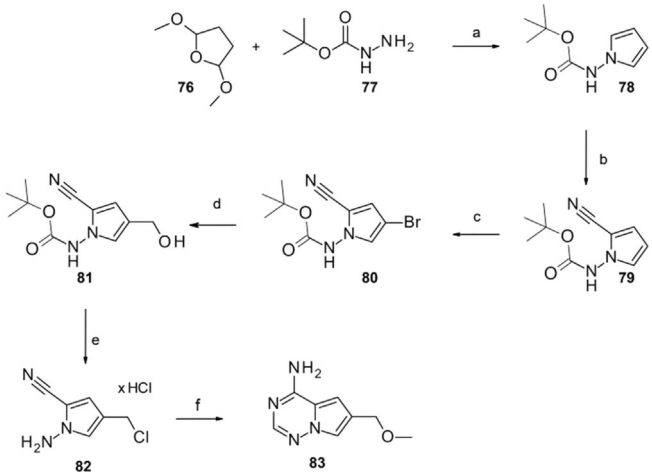

Scheme 1. a) HCl, dioxane, 90 °C, 41%; b) chlorosulfonylisocyanate, acetonitrile, DMF, 0 °C, 96%; c) NBS, DMF, −5 °C, 89%; d) 1. MeMgBr, 2-Me-THF, −60 °C, 2. *n*BuLi, −60 °C, 3. paraformaldehyde, RT, 69%; e) 4 M HCl/dioxane, RT; f) formamidine acetate, K_3PO_4, MeOH, reflux, 49% (two steps).

benzothiophene via a Suzuki coupling. This synthetic route was realized as depicted in Schemes 1–3, and comprises ten linear steps in a convergent synthesis.[11] The pyrrolotriazine core structure **83** was prepared in 6 linear steps (Scheme 1). The synthesis started with an acid-catalyzed condensation reaction of the commercially available 2,5-dimethoxytetrahydrofuran (**76**) with *tert*-butyl carbazate (**77**) affording, after crystallization, the protected aminopyrrole **78** in a yield of 41%.

Introduction of the nitrile group at C1 by electrophilic substitution using chlorosulfonylisocyanate followed by intramolecular elimination afforded cyanopyrrole **79** (96%). Bromination at C4 of pyrrole **79** with *N*-bromosuccinimide was performed at 0 °C to increase the desired regioselectivity and prevent overreaction (dibromination), thus leading to bromo-pyrrole **80** in a yield of 89%. The hydroxymethyl group was then installed in a subsequent three-step one-pot reaction. At −60 °C, the NH of bromide **80** was first deprotonated with methylmagnesium bromide, followed by lithium–bromide exchange with *n*-butyllithium. Quenching with paraformaldehyde at room temperature led to hydroxymethylpyrrole **81** in 69% yield (three steps). Treating the pyrrole **81** with a hydrogen chloride solution in dioxane not only cleaved the *tert*-butylcarbamate group, but also converted the hydroxymethyl group into the corresponding chloromethyl **82**. This very reactive intermediate **82** could be directly converted into the methoxymethylpyrrolotriazine **83** in a one-pot, two-step reaction sequence by treating **82** with methanol, followed by formamidine acetate and potassium phosphate at reflux temperature (49%, two steps).

In parallel, the boronic acid **89** was synthesized in five linear steps (Scheme 2). The synthesis started with the hydrogenation of nitro anisole **84** to afford aniline **85** using palladium on activated charcoal under an atmosphere of hydrogen. Aniline **85**

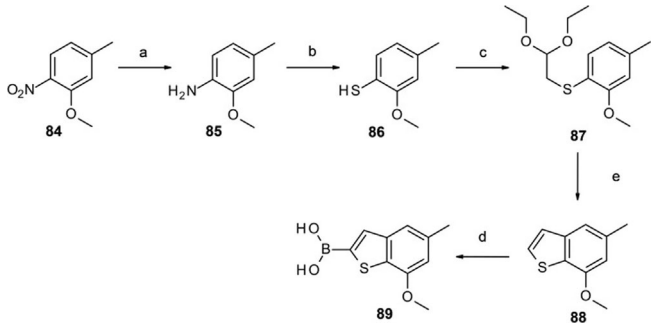

Scheme 2. a) H_2, Pd/C, THF, RT; b) 1. $NaNO_2$, HCl, NaOAc, 0 °C, 2. KCS_2OEt, water, 80 °C, 3. KOH, EtOH, reflux; c) bromoacetaldehyde diethylacetal, Cs_2CO_3, DMF, RT, 66% (three steps); d) polyphosphoric acid, chlorobenzene, reflux, 49%; e) 1. *n*BuLi, THF, −70 °C, then B(O*i*Pr)$_3$, 2. aq. NaOH (2 N), 80%.

was converted into the corresponding diazonium salt, which was treated with a hot aqueous solution of potassium ethylxanthogenate. Finally, saponification with potassium hydroxide led to the desired thiophenol **86**, which was immediately alkylated with bromoacetaldehyde diethylacetal in the presence of cesium carbonate to obtain the more stable thioether **87** in an overall yield of 66% from nitroanisole **84**. Thioether **87** was cyclized to the corresponding benzothiophene **88** using polyphosphoric acid in chlorobenzene at elevated temperature (49% yield). Finally, deprotonation of benzothiophene **88** at C2 with *n*-butyllithium in THF, reaction with triisopropylborate and subsequent hydrolysis afforded boronic acid **89** in a good yield of 80%.

The final assembly started with a Vilsmeier formylation of **83** at C7 to afford aldehyde **90** (26%, Scheme 3). The moderate yield of the reaction was mainly due to the strong acidic reaction conditions which led to the partial cleavage of the methoxy group. Aldehyde **90** was then reacted with *N*-bromosuccinimide at 0 °C to afford C5-bromo analogue **91** in 94% yield. The coupling of bromide **91** with the boronic acid **89** under thoroughly optimized Suzuki–Miyaura conditions afforded the corresponding benzothiophene **92** in a yield of 51%. The best coupling conditions were obtained with the X-Phos precatalyst.[12] Other catalysts, such as the corresponding S-Phos pre-

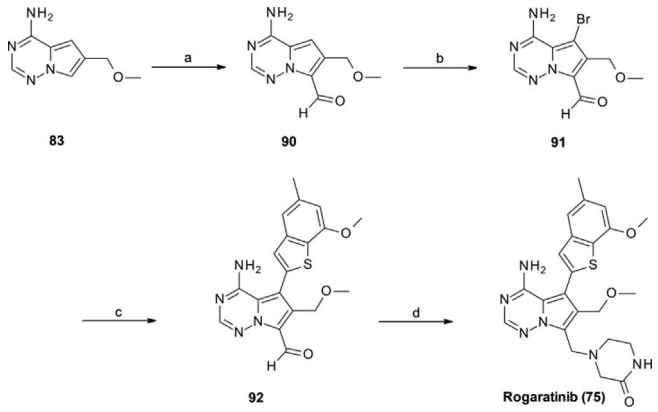

Scheme 3. a) $POCl_3$, DMF, 60 °C, 26%; b) NBS, DMF, 0 °C; 94%; c) **89**, X-Phos precatalyst, CsF, THF, water, 60 °C, 51%; d) piperazinone, $NaBH(OAc)_3$, AcOH, MeOH, 60 °C, 14%.

catalyst, gave lower yields or no conversion. The optimization of the base was also important to prevent proto-deboronation of **89** during the reaction. Cesium fluoride was identified as the most suitable base for our purpose. Finally, reductive amination of aldehyde **92** with piperazine-2-one in the presence of sodium triacetoxyborohydride as reducing agent led to rogaratinib (**75**) in 14% yield.

Conclusions

Using a computational chemistry approach to generate lead compounds, we have presented the discovery of rogaratinib (**75**), a novel small-molecule inhibitor of FGFR1–4. Rogaratinib has good DMPK properties. It demonstrated tumor growth reduction in pre-clinical models bearing different FGFR alterations both in mono- and combination therapy.[13] Rogaratinib is currently being evaluated in phase I clinical trials (NCT 01976741).

Experimental Section

All experimental data are shown in the Supporting Information.

Acknowledgements

The authors thank their co-workers for their dedication and skillful work. The contributions by service functions of the various institutes are also gratefully acknowledged. Furthermore, we thank the clinical development team for continuous support of this project.

Conflict of interest

The authors declare no conflict of interest.

Keywords: cancer · structure-based design · fibroblast growth factor receptor (FGFR) · inhibitors · medicinal chemistry

[1] D. M. Ornitz, N. Itoh, *WIREs Dev. Biol.* **2015**, *4*, 215 – 266.
[2] R. Ronca, A. Giacomini, M. Rusnati, M. Presta, *Exp. Opin. Ther. Targets* **2015**, *19*, 1361 – 1377.
[3] a) S. Saichaemchan, W. Ariyawutyakorn, M. Varella-Garcia, *Curr. Mol. Med.* **2016**, *16*, 40 – 62; b) N. Hallinan, S. Finn, S. Cuffe, S. Rafee, K. O'Byrne, K. Gyle, *Cancer Treat. Rev.* **2016**, *46*, 51 – 62; c) C. Hierro, J. Rodon, J. Tabernero, *Semin. Oncol.* **2015**, *42*, 801 – 819; d) L. Korsensky, D. Ron, *Semin. Cell Dev. Biol.* **2016**, *53*, 101 – 114; e) G. Liang, G. Chen, X. Wei, Y. Zhao, X. Li, *Cytokine Growth Factor Rev.* **2013**, *24*, 467 – 475; f) B. V. S. S. Kumar, L. Narasu, R. Gundla, R. Dayam, J. A. R. P. Sarma, *Curr. Pharm. Des.* **2013**, *19*, 687 – 701; g) M. V. Dieci, M. Arnedos, F. Andre, J. C. Soria, *Cancer Discovery* **2013**, *3*, 264 – 279; h) J. Wesche, K. Haglund, E. M. Haugsten, *Biochem. J.* **2011**, *437*, 199 – 213.
[4] P. Gavine, L. Mooney, E. Kilgour, A. P. Thomas, K. Al-Kadhimi, S. Beck, C. Rooney, T. Coleman, D. Baker, M. J. Mellor, A. N. Brooks, T. Klinowska, *Cancer Res.* **2012**, *72*, 2045 – 2056.
[5] a) J. Tabernero, R. Bahleda, R. Dienstmann, J. R. Infoante, A. Mita, A. Italiano, E. Calvo, V. Moreno, B. Adamo, A. Gazzah, B. Zhong, S. J. Platero, J. W. Smit, K. Stuyckens, M. Chatterjee-Kishore, J. Rodom, V. Peddareddigari, F. R. Luo, J.-C. Soria, *J. Clin. Oncol.* **2015**, *33*, 3401 – 3408; b) R. Dienstmann, R. Bahleda, B. Adamo, J. Rodon, A. Varga, A. Gazzah, S. Platero, H. Smit, T. Perera, B. Zhong, K. Stuyckens, Y. Elsayed, C. Takimoto, V. Peddareddigari, J. Tabernero, F. Roger Luo, J. C. Soria, American Association for Cancer Research (AACR) 106th Annual Meeting, April 5 – 9, 2014 (San Diego, CA, USA), Abstract CT326; c) P. R. Angibaud, L. Mevellec, G. Saxty, C. Adelinet, R. Akkari, V. Berdini, et al., American Association for Cancer Research (AACR) 106th Annual Meeting, April 5 – 9, 2014 (San Diego, CA, USA), Abstract 4748.
[6] A. Hillisch, N. Heinrich, H. Wild, *ChemMedChem* **2015**, *10*, 1958 – 1962.
[7] M. Mohammadi, S. Froum, J. M. Hamby, M. C. Schroeder, R. L. Panek, G. H. Lu, A. V. Eliseenkova, D. Green, J. Schlessinger, S. R. Hubbard, *EMBO J.* **1998**, *17*, 5896 – 5904.
[8] R. Abel, T. Young, R. Farid, B. J. Berne, R. A. Friesner, *J. Am. Chem. Soc.* **2008**, *130*, 2817 – 2831.
[9] T. Young, R. Abel, B. Kim, B. J. Berne, R. A. Friesner, *Proc. Natl. Acad. Sci. USA* **2007**, *104*, 808 – 813.
[10] M. A. Fabian, W. H. Biggs III, D. K. Treiber, C. E. Atteridge, M. D. Azimioara, M. G. Benedetti, T. A. Carter, P. Ciceri, P. T. Edeen, M. Floyd, J. M. Ford, M. Galvin, J. L. Gerlach, R. M. Grotzfeld, S. Herrgard, D. E. Insko, M. A. Insko, A. G. Lai, J.-M. Lélias, S. A. Mehta, Z. V. Milanov, A. M. Velasco, L. M. Wodicka, H. K. Patel, P. P. Zarrinkar, D. J. Lockhart, *Nat. Biotechnol.* **2005**, *23*, 329 – 336.
[11] D. Brohm, M. Héroult, M.-P. Collin, W. Hübsch, M. Lobell, K. Lustig, S. Grünewald, U. Bömer, V. Voehringer (Bayer Pharma Aktiengesellschaft), Int. PCT Pub. No. WO2013087578, **2013**.
[12] T. Kinzel, Y. Zhang, S. L. Buchwald, *J. Am. Chem. Soc.* **2010**, *132*, 14073 – 14075.
[13] a) M. Héroult, P. Ellinghaus, C. Sieg, D. Brohm, S. Grünewald, M.-P. Collin, U. Bömer, M. Lobell, W. Hübsch, M. Ocker, S. Ince, R. Jautelat, H. Hess-Stumpp, M. Brands, K. Ziegelbauer, American Association for Cancer Research (AACR) 106th Annual Meeting, April 5 – 9, 2014 (San Diego, CA, USA), Abstract 1739; b) M. Héroult, M. Ocker, C. Kopitz, D. Zopf, A. Hägebarth, K. Ziegelbauer, S. Ince, P. Ellinghaus, American Association for Cancer Research (AACR) 107th Annual Meeting, April 18 – 22, 2015 (Philadelphia, PA, USA), Abstract 772; c) M.-P. Collin, M. Lobell, D. Brohm, W. Hübsch, R. Jautelat, S. Jaroch, M. Brands, M. Héroult, S. Grünewald, U. Bömer, H. Hess-Stumpp, K. Ziegelbauer, American Association for Cancer Research (AACR) 108th Annual Meeting, April 16 – 20, 2016 (New Orleans, LA, USA), Abstract 4332.

Manuscript received: November 16, 2017
Revised manuscript received: January 20, 2018
Accepted manuscript online: ■■ ■■, 0000
Version of record online: ■■ ■■, 0000

M.-P. Collin, M. Lobell, W. Hübsch, D. Brohm, H. Schirok, R. Jautelat, K. Lustig, U. Bömer, V. Vöhringer, M. Héroult, S. Grünewald, H. Hess-Stumpp*

■■ – ■■

Discovery of Rogaratinib (BAY 1163877): a pan-FGFR Inhibitor

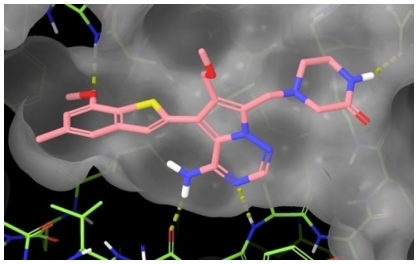

In phase 1: We disclose the discovery and chemical structure of rogaratinib (BAY 1163877), a highly potent and selective pan-FGFR inhibitor currently being assessed in clinical trials for the treatment of cancer. We describe the structure–activity relationship and the pharmacokinetic profile of the benzothiophenyl-pyrrolotriazine structure class.